Nano Research

Open Access

Research Article

Water enhances photocatalytic activity for toluene selective oxidation in acetic acid solution

Sheng Tian[1], Jinxin Li[1], Binghao Wang[1], Xiong Wang[1], Xingsheng Hu[1], Huijuan Wang[1], Lang Chen[1] ✉, and Shuang-Feng Yin[1,2] ✉

[1] *Advanced Catalytic Engineering Research Center of the Ministry of Education, State Key Laboratory of Chemo/Biosensing and Chemometrics, College of Chemistry and Chemical Engineering, Hunan University, Changsha 410082, China*
[2] *College of Chemistry and Chemical Engineering, Central South University of Forestry and Technology, Changsha 410004, China*

Cite this article: *Nano Research*, **2025**, *18*, 94907206. https://doi.org/10.26599/NR.2025.94907206

ABSTRACT: Photocatalytic oxidation of hydrocarbons to value-added oxygen-containing compounds is a green and sustainable method. However, the efficient activation of C(sp^3)–H bonds under mild conditions remains a significant challenge. In this study, we prepared $BiOBr/Bi_2MoO_6$ Z-scheme heterostructure for photocatalytic selective oxidation of toluene to benzaldehyde utilizing acetic acid as solvent. A small amount of water as an additive established an acidic environment to facilitate the formation of highly reactive hydroxyl radicals (·OH) through the $O_2 \rightarrow \cdot O_2^- \rightarrow H_2O_2 \rightarrow \cdot OH$ process. The ·OH together with photogenerated holes acted as reactive species dissociate C(sp^3)–H bonds, which is regarded as the rate-determining step for this reaction, boosting photocatalytic activity. Compared to the reaction system without water, the conversion of toluene increased from 23.6% to 39.0%, reaching a toluene conversion rate of 6110 μmol·g^{-1}·h^{-1}. Additionally, there is a slight improvement in the selectivity of benzaldehyde.

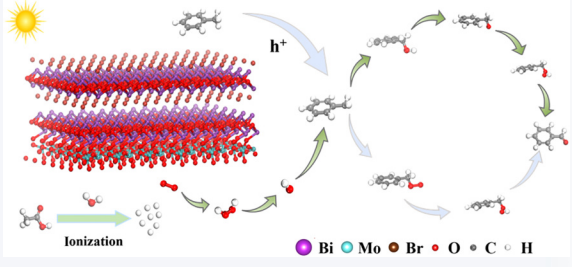

KEYWORDS: photocatalytic oxidation of toluene, H_2O, acidic chemical environment, hydroxyl radicals, $BiOBr/Bi_2MoO_6$

1 Introduction

The progress of chemical industry relies heavily on research of selective activation and transformation of C(sp^3)–H bonds to generate valuable compounds [1, 2]. However, the activation of C(sp^3)–H bonds often requires harsh conditions such as high temperatures, high pressures, and strong oxidants, leading to substantial energy consumption and environmental damage [3]. In recent years, there has been a remarkable surge in interest in photocatalytic organic synthesis, which was regarded as a green and sustainable method. One illustrative example is the photocatalytic oxidation of toluene to produce benzaldehyde. In the photocatalytic oxidation reaction of toluene, dissociation of the C(sp^3)–H bonds to form benzyl radical was regarded as the rate-determining step, which was typically achieved through holes oxidation or active radical oxidation [4, 5]. In photocatalytic reactions, reactive oxygen species (ROS) were served as the primary oxidants in addition to photogenerated holes in photooxidation reactions [6–9]. Activating the C(sp^3)–H bonds through the combined action of ROS and holes may be a viable strategy for enhancing the oxidation activity of toluene.

Among various ROS including hydroxyl radicals (·OH), superoxide radicals ($\cdot O_2^-$), and singlet oxygen ($^1O_2$), ·OH possess the strongest oxidation capacity and can directly activate the C(sp^3)–H bonds of toluene [10–12]. Recently, researchers have proposed a strategy of utilizing photogenerated holes to oxidize H_2O into ·OH, which can then facilitate the conversion of organic compounds. In a study conducted by Jiang et al., the addition of water in acetonitrile solvent was observed to enhance the conversion of toluene significantly [13]. Later, the photocatalytic transformation of ethylbenzene was also achieved using a mixed solvent of water and tert-butyl alcohol [14]. This significant breakthrough was facilitated by the generation of ·OH through the process of photocatalysis. However, the oxidation of H_2O to generate ·OH requires a high oxidation potential (E = 2.38 V vs. standard hydrogen electrode (SHE)) [15, 16]. Additionally, this process consumes a significant number of photogenerated holes, making it a big challenge to activate organic substrates solely through hole oxidation. It is evident that the incorporation of H_2O_2 into the photocatalytic system can generate ·OH, thereby enhancing the reactivity of photocatalytic process [17, 18]. However, directly adding H_2O_2 into the reaction system can make the reaction process uncontrollable

Received: October 21, 2024; **Revised:** December 17, 2024
Accepted: December 20, 2024

✉Address correspondence to Lang Chen, huagong042cl@163.com; Shuang-Feng Yin, sf_yin@hnu.edu.cn

and increase the cost. It has been observed that under an acidic chemical environment, a continuous two-electron process can reduce O_2 to H_2O_2, which can subsequently decompose to form ·OH [19–21]. Meanwhile, in the context of toluene oxidation, researchers have investigated the performance of thermal catalysts in various solvents and found that the highest toluene oxidation performance was achieved in acetic acid, followed by acetonitrile, and then ethyl acetate [22]. The polarity and acidity of solvent were proved to play a crucial role in determining the oxidation performance of toluene. Therefore, employing acetic acid as a solvent for the photocatalytic oxidation of toluene, with the addition of water to facilitate the ionization of acetic acid and generate H_2O_2 in an acidic environment, followed by the decomposition of H_2O_2 to produce ·OH, represents an effective strategy for enhancing the activity of toluene photooxidation.

In recent years, Bi-based semiconductors have garnered significant attention from researchers due to their favorable band structure and cost-effective availability. They have found extensive applications in the field of photocatalysis, including water splitting, CO_2 reduction, N_2 fixation, and organic synthesis [23–25]. Among them, Bi_2MoO_6 (BMO) exhibits a distinctive layer-like structure composed of alternating $Bi_2O_2^{2+}$ and MoO_4^{2-} layers, and it crystallizes in the orthorhombic crystal system [26, 27]. The distinctive structure of Bi_2MoO_6, along with its favorable valence and conduction band potentials, has positioned it as a promising candidate material for photocatalytic selective conversion of organic compounds [28, 29]. In our previous work, Bi_2MoO_6 nanocrystals with varying thicknesses were synthesized for the purpose of selective toluene photooxidation. The reduced thickness of nanocrystals facilitated the rapid separation of photogenerated electron-hole pairs, minimizing the likelihood of recombination [30]. In a recent study, two-dimensional (2D) $Bi_2W_{0.3}Mo_{0.7}O_6$ was fabricated by Dai et al. and it exhibited good photocatalytic activity for benzaldhyde formation. The improved photocatalytic activity of $Bi_2W_{0.3}Mo_{0.7}O_6$ was attributed to its balanced charge kinetics and optimized band structure [31]. Moreover, Bi_2MoO_6 exhibits a good affinity for oxygen, enabling the conversion of O_2 to H_2O_2 [32, 33]. However, the efficiency of charge carrier separation in Bi_2MoO_6, especially its bulk components, still requires enhancement. Consequently, a composite photocatalyst based on 2D Bi_2MoO_6 stands out as a viable option for the reduction of O_2 to hydrogen peroxide via the conduction band, and for the generation of hydroxyl radicals, while concurrently oxidizing toluene to benzaldehyde through the valence band holes.

In this study, we synthesized BiOBr (BOB)/Bi_2MoO_6 Z-scheme heterostructure for photocatalytic toluene oxidation using acetic acid as a solvent. The construction of heterostructure between BiOBr and Bi_2MoO_6 facilitated the separation of photogenerated carriers. A small amount of water as an additive in the reaction system created an acidic chemical environment, which benefited the transformation of $\cdot O_2^-$ to ·OH through the $O_2 \rightarrow \cdot O_2^- \rightarrow H_2O_2 \rightarrow$ ·OH process. This transformation of ROS boosted the photocatalytic conversion of toluene. Simultaneously, the presence of water facilitates the conversion of benzyl alcohol to benzaldehyde, resulting in a slightly improved selectivity towards benzaldehyde.

2 Experimental

2.1 Chemicals

Bismuth nitrate pentahydrate ($Bi(NO_3)_3·5H_2O$), sodium molybdate dihydrate ($NaMoO_4·2H_2O$), potassium iodide (KI), cetyltrimethylammonium bromide (CTAB), toluene ($C_6H_5CH_3$), and acetic acid (CH_3COOH) were obtained from Sinopharm Chemical Reagent Co. Ltd., Shanghai, China. All reagents were of analytical grade and used without further purification. Deionized water used throughout the experiments was homemade with a resistivity of 18.2 MΩ·cm.

2.2 Catalyst synthesis

The BiOBr/Bi_2MoO_6-X (X = 1, 2, 3, 4) composites were fabricated via a one-step hydrothermal method. Specifically, 2 mmol of $Bi(NO_3)_3·5H_2O$, 1 mmol of $Na_2MoO_4·2H_2O$, and a certain amount of CTAB were added to 80 mL of deionized water. After stirring for 30 min, the mixture was placed into a 100 mL Teflon-lined stainless steel autoclave and treated at 180 °C for 8 h. Subsequently, the sample was washed several times with deionized water and absolute ethanol, followed by drying in air at 80 °C overnight. The resulted samples were defined as BOB/BMO-X (X = 1, 2, 3, 4), where X represent the amount of CTAB (0.1, 0.2, 0.3, and 0.4 g, respectively) during the synthesis process. BMO was also prepared using the same method without adding CTAB. For a typical synthesis of BOB, 2 mmol of $Bi(NO_3)_3·5H_2O$ and 2 mmol of KBr were dissolved in 30 mL of deionized water. After stirring for an additional 30 min, the suspension was transferred to a 50 mL Teflon-lined stainless steel autoclave and heated at 160 °C for 24 h. Once cooled down to room temperature naturally, the final product was collected by centrifuging, washed three times with deionized water and absolute ethanol, and dried in air at 80 °C overnight.

2.3 Characterization

Crystal structure of the prepared catalysts was analyzed using X-ray diffraction (XRD) over a SHIMADZU XRD-6100 instrument using Cu Kα radiation (λ = 0.15406 nm). To analyze the morphology and elemental distribution, scanning electron microscopy (SEM, Hitachi S-4800) and transmission electron microscopy (TEM, JEOL JEM-2100F) equipped with energy-dispersive X-ray (EDX) were used. To obtain the surface composition and chemical states of elements, X-ray photoelectron spectroscopy (XPS, PHI VersaProbe 4) was employed using Mg Kα radiation ($h\nu$ = 1253.6 eV). Ultraviolet–visible diffuse reflectance spectra (UV–vis DRS) were measured through a Cary-100 spectrophotometer. The photoluminescence (PL) spectra were acquired on a fluorescence spectrometer (Hitachi, F-4600). Time resolved PL decay curves were recorded on an Edinburgh FLS1000 fluorescence lifetime spectrophotometer. Electron spin resonance (ESR, Bruker EMXplus) spectroscopy was used to detect the active species produced during the reaction process. *In situ* diffuse reflection infrared Fourier transform spectroscopy (*in situ* DRIFTS) was performed using a Bruker TENSOR II Fourier transform infrared spectroscopy (FTIR) NEXUS. First, catalysts were heated under N_2 flow from room temperature to 120 °C for 5 min to remove the absorbed water. Under dark conditions, N_2 containing toluene (200 ppm), oxygen, and water was introduced into the chamber and pre-adsorbed on the catalyst surface for 20 min. Measurements were taken every 4 min, resulting in 5 testing curves. After the gas introduction was stopped, the xenon lamp was turned on for visible light irradiation for 30 min, and measurements were taken every 5 min resulting in an additional 6 testing curves. Transient photocurrent, electrochemical impedance spectroscopy (EIS), and Mott–Schottky (M–S) plots were conducted using an

electrochemical workstation (CHI 660E) in a three-electrode system comprising fluorine-doped tin oxide (FTO) as the working electrode, a platinum sheet as the counter electrode, and Ag/AgCl as the reference electrode. The FTO conductive glass was sequentially cleaned by sonication for 30 min with toluene, acetone, ethanol, and water. 5 mg of catalyst was dispersed in 5 mL of ethanol, and 10 μL of Nafion was added. The mixture was then sonicated for 30 min and drop-casted onto FTO (1 cm × 1 cm) glass and dried at room temperature for 12 h. To conduct the photoelectrochemical test, a 0.5 M Na_2SO_4 solution was used as the electrolyte.

2.4 Photocatalytic performance evaluation

The photocatalytic toluene oxidation reaction was conducted in a 25 mL Schlenk flask with a branch pipe. In a typical procedure, 10 mg of photocatalyst, 50 μL of toluene, 2 mL of acetic acid, and a certain amount of deionized water were added to the Schlenk flask. The air present in the Schlenk flask was removed through the oil pump equipped with a double-row tube under liquid nitrogen refrigeration. The O_2 was introduced into the reaction system through the branch pipe of the Schlenk flask with an O_2 balloon. Before visible light irradiation, the mixture was stirred for 30 min to achieve adsorption–desorption equilibrium. The photocatalytic reaction occurred under the irradiation of visible light emitted by a 300 W xenon lamp with a 400 nm cutoff filter, with continuous stirring for 3 h. The products were analyzed using a Shimadzu GC-2010Plus gas chromatograph equipped with an FID and a 1701 capillary column using chlorobenzene as the internal standard substance. The H_2O_2 concentration was determined through a cerium sulfate ($Ce(SO_4)_2$) titration method. The linear relationship between Ce^{4+} concentration and the absorption intensity was depicted in Fig. S1 in the Electronic Supplementary Material (ESM).

2.5 Computational methods

All the density functional theory (DFT) calculations were performed using the Vienna *ab-initio* simulation package (VASP) [34]. The project-augmented wave (PAW) method was applied to describe the core-valence interaction [35]. The Perdew–Burke–Ernzerhof (PBE) functional, which uses the generalized gradient approximation (GGA), was employed to handle the exchange and correlation potential [36]. A cutoff energy of 450 eV with an energy convergence threshold of 1×10^{-5} eV and a force convergence criterion of 0.02 eV·Å^{-1} were used. To avoid the interaction between neighboring layers, a 15 Å vacuum layer in the *z*-direction was set. A 3 × 3 × 1 k-mesh of the Brillouin zone was employed.

3 Results and discussion

3.1 Morphology and structure

XRD patterns of synthesized BOB and BMO displayed characteristic peaks corresponding to the tetragonal phase BiOBr (PDF#09-0309) and orthorhombic phase Bi_2MoO_6 (PDF#21-0102), respectively, with no detection of other impurities (Fig. 1(a)). In the case of BOB/BMO-*X* samples, similar patterns to those of BMO were detected, with no peaks belonging to BOB appeared when the amount of CTAB is lower than 0.2 g (BOB/BMO-2). Characteristic peaks of BOB located at 31.7° and 57.2° in the composite, ascribing to the (102) and (212) planes, appeared with the CTAB amount as high as 0.3 g. This phenomenon indicates the success in fabrication of BOB/BMO composite and the amount of BOB depends on CTAB involved in synthesis. All prepared samples are of sheet-like structure (Figs. 1(b) and 1(c) and Fig. S2 in the ESM), but the incorporation of CTAB had a notable effect on reducing the thickness of resulted composites. TEM images confirmed the nanosheet structure of BOB/BMO-3 (Fig. 1(d)) with lattice spacings of 0.274 and 0.282 nm correspond to (002) plane of BMO and (102) plane of BOB (Fig. 1(e)), respectively. The homogeneous distribution of Bi, Mo, O, and Br elements (Figs. 1(f)–1(j)) according to EDX analysis, further confirms.

XPS was employed to examine the chemical state of surface

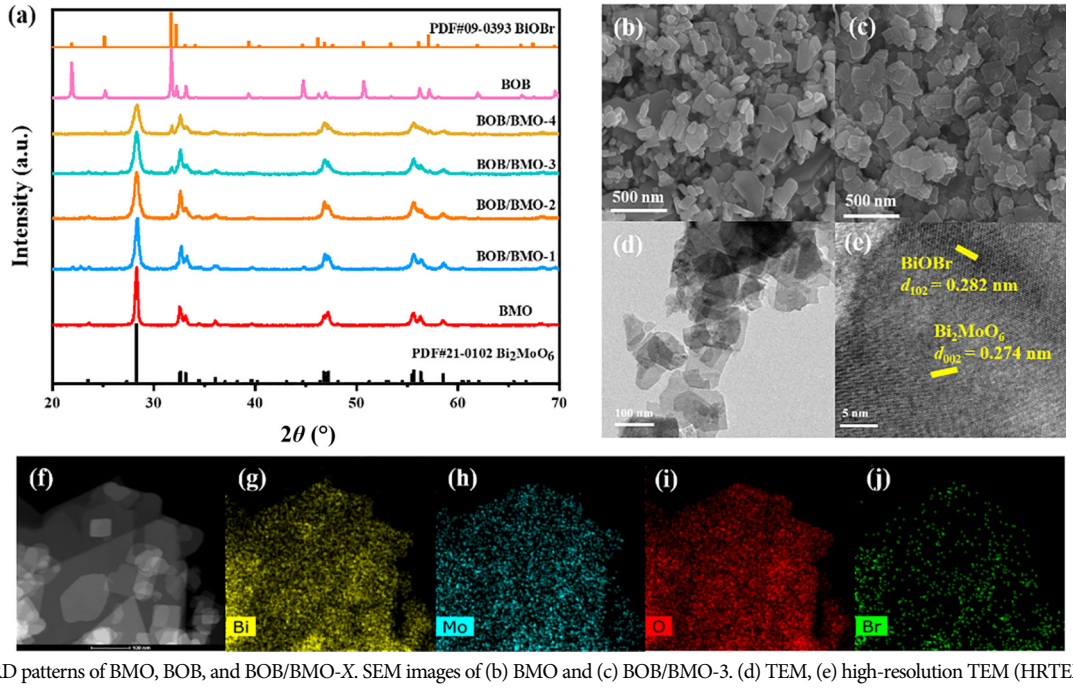

Figure 1 (a) XRD patterns of BMO, BOB, and BOB/BMO-*X*. SEM images of (b) BMO and (c) BOB/BMO-3. (d) TEM, (e) high-resolution TEM (HRTEM), and (f) high-angle annular dark-field scanning TEM (HAADF-STEM) images, and (g)–(j) corresponding elemental mappings of BOB/BMO-3.

elements. The peaks observed at 164.6 and 159.3 eV corresponded to Bi $4f_{5/2}$ and Bi $4f_{7/2}$ (Fig. S3(a) in the ESM), respectively, indicating Bi in the prepared samples present at +3 [37]. Similarly, peaks at 235.8 and 232.6 eV were attributed to Mo $3d_{5/2}$ and Mo $3d_{7/2}$ (Fig. S3(b) in the ESM), respectively, suggesting the presence of Mo^{6+} [38]. The addition of CTAB did not cause a shift in peak position of Bi 4f and Mo 3d, which was consistent with previous reports [39]. The observed O 1s XPS peak at 530.3 eV was assigned to lattice oxygen, while the one at 532.2 eV for BMO was attributed to the adsorbed oxygen, which originated from the adsorption of O_2/H_2O on the catalyst surface [40]. Notably, the presence of an additional peak at 531.6 eV, corresponding to bridging hydroxyls, was exclusively observed for BOB/BMO-3 (Fig. S3(c) in the ESM) [41]. Br 3d peak located at 68.9 eV appeared over BOB/BMO-3 but was absent on BMO (Fig. S3(d) in the ESM). Combined with the results of XRD and XPS analysis, successful preparation of BOB/BMO composite was confirmed.

Optical property of prepared samples was characterized using UV–vis DRS. All prepared samples are of visible light response and bandgap energy (E_g) values of BOB, BMO, and BOB/BMO-3 were calculated to be 2.74, 2.36, and 2.41 eV, respectively (Figs. S4(a) and S4(b) in the ESM). The flat-band potentials of BOB and BMO were measured to be −0.62 and −0.10 V (vs. Ag/AgCl), respectively, according to M–S plots (Figs. S4(c) and S4(d) in the ESM). Correspondingly, the conduction band (CB) position relative to the normal hydrogen electrode (NHE) was determined to be −0.42 V for BMO and +0.10 V for BOB, with valence band (VB) position calculated to be +1.94 and +2.84 V for BMO and BOB, respectively.

3.2 Electronic structure and photoelectrochemical properties

DFT was used to analyze electronic structure of BOB/BMO heterostructure, and the structural model of BOB/BMO heterostructure was depicted in Fig. S5 in the ESM. The density of states (DOS) was calculated within the energy range of −4 to 4 eV (Fig. 2(a)). It was evident that the valence band maximum of the BOB/BMO heterostructure was predominantly contributed by O of BMO, while the conduction band minimum was mainly contributed by Bi in BOB, suggesting that the BOB/BMO heterostructure exhibited a staggered band alignment. Additionally, the work functions of BMO and BOB were calculated to be 4.71 and 7.02 eV, respectively, indicating a higher Fermi level of BMO than that of BOB (Figs. 2(b) and 2(c)). The charge density difference of BOB/BMO heterostructure was calculated by the following Eq. (1) [42, 43]

$$\Delta\rho = \rho_{BOB/BMO} - \rho_{BOB} - \rho_{BMO} \quad (1)$$

where $\rho_{BOB/BMO}$, ρ_{BOB}, and ρ_{BMO} are charge densities of BOB/BMO heterostructure, BOB, and BMO, respectively. It is clearly observed that electrons are predominantly accumulated on one side of the BOB layer, with a directional transfer of electrons occurring from BMO to BOB at the heterojunction interface (Figs. 2(d) and 2(e)). Based on the findings from UV–vis DRS, Mott–Schottky analysis, and work function determination, the energy band alignment and charge transfer mechanism of the heterostructure was elucidated in Fig. 2(f). Upon contact between BMO and BOB, the formation of an internal electric field and band bending enables the alignment of Fermi levels. When catalyst was irradiated, both BMO and BOB became excited, leading to the generation of electron–hole pairs. Benefiting from the internal electric field, band bending, and Coulomb force, the photogenerated electrons in the CB of BOB will combine with the photogenerated holes in the VB of BMO. As a result, holes accumulate in the VB of BOB, and electrons accumulate in the CB of BMO. This Z-scheme charge transfer mechanism facilitates efficient separation of photogenerated charge carriers, preserving their strong redox abilities, i.e., capable of O_2 reduction into $\cdot O_2^-$ and water oxidation in giving ·OH.

Compared to BMO and BOB, BOB/BMO-3 demonstrated an enhanced transient photocurrent density, indicating more effective separation of photogenerated charge carriers (Fig. 3(a)). The EIS plot of BOB/BMO-3 exhibited a smaller semicircle radius, indicating a lower interface resistance (Fig. 3(b)). In addition, BOB/BMO-3 exhibited much lower intensity of PL emission compared to BOB and BMO, further confirming its higher carrier separation efficiency (Fig. 3(c)). Moreover, average fluorescence lifetime of BOB/BMO-3 (τ_{ave} = 3.46 ns) was longer than that of

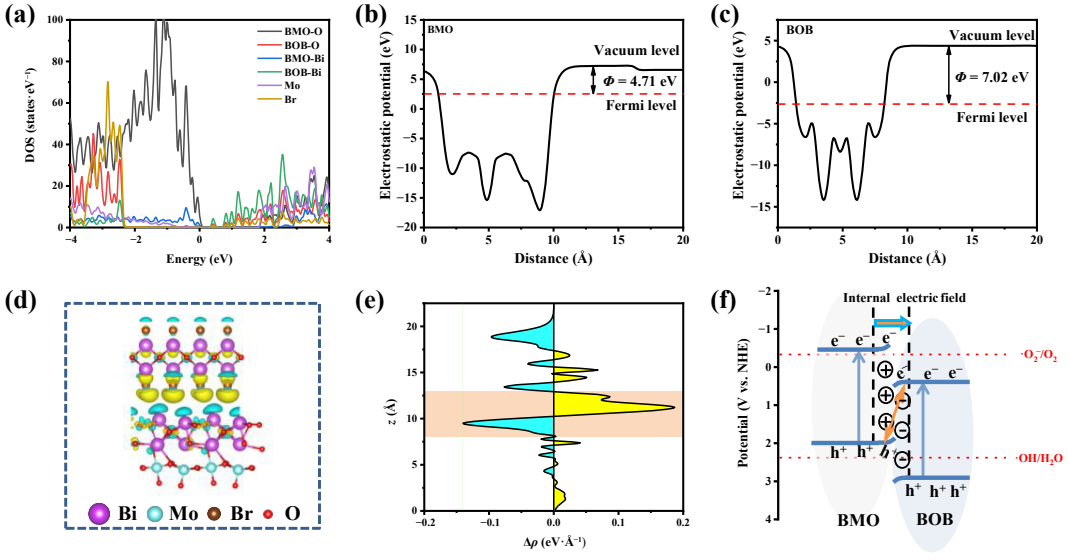

Figure 2 (a) Projected DOS (PDOS) of BOB/BMO. The electrostatic potentials of (b) BMO and (c) BOB. (d) The charge density difference and (e) planar-averaged differential charge densities $\rho(z)$ of BOB/BMO, the blue and yellow isosurfaces stand for electron depletion and electron accumulation, respectively. (f) Schematic diagram of band alignment and charge separation at the interface of BOB/BMO.

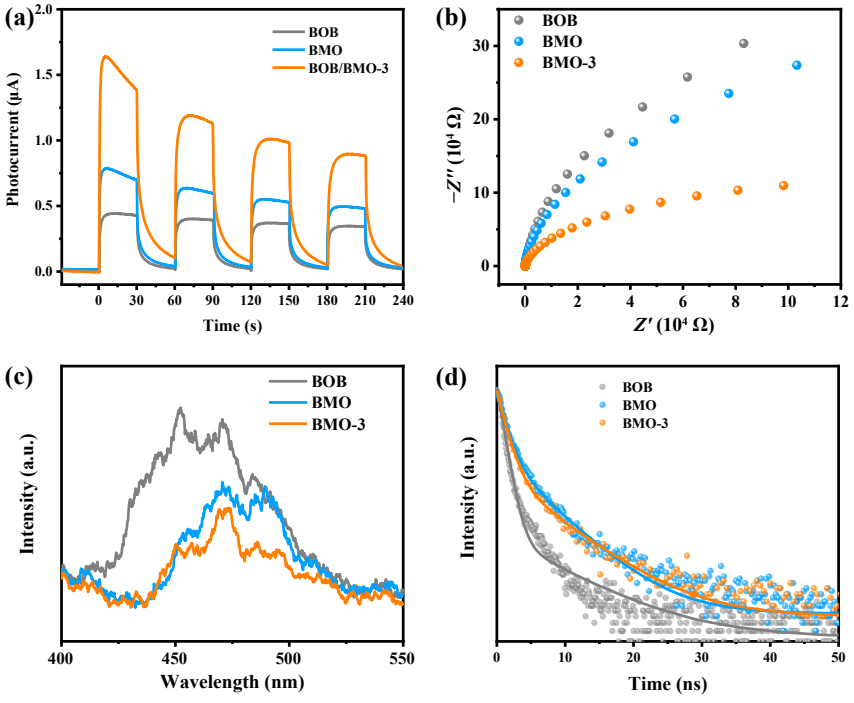

Figure 3 (a) Transient photocurrent response, (b) electrochemical impedance spectra, (c) steady-state PL spectra, and (d) TRPL decay spectra of BOB, BMO, and BOB/BMO-3.

BMO (τ_{ave} = 3.33 ns) according to the time-resolved photoluminescence (TRPL) decay spectra, indicating superior charge migration property along the Z-scheme heterostructure of BOB/BMO-3 (Fig. 3(d)).

3.3 Photocatalytic property

The selective oxidation of toluene under visible light in acetic acid was used to evaluate the performance of the prepared catalysts (Fig. 4(a)). Pure BMO exhibited low photocatalytic activity, with only toluene conversion of 1.5% after 3 h of light irradiation. However, there was a significant improvement in the toluene conversion over all BOB/BMO composites. Among them, BOB/BMO-3 exhibited the highest conversion of 23.6%, and benzaldehyde was the main product with a selectivity of 81.5%. When BOB was used as the catalyst, the conversion rate of toluene was 13.3%, and the selectivity for benzaldehyde was 85.3%. Surprisingly, a small amount of water in the reaction system further enhanced catalytic activity (Fig. 4(b)). Toluene conversion reached 39.0% accompanied by a benzaldehyde selectivity of 84.2% when an optimized amount of water (0.2 mL) was added. Slightly increased benzaldehyde selectivity (81.6% to 84.2%) in the presence of water could be ascribed to enhanced capacity for converting benzyl alcohol (selectivity from 10.4% to 6.7%) to benzaldehyde, which is consistent with the results of previous studies [44, 45]. With an extended reaction time, the conversion of toluene exhibits an upward trend, with the amount of benzaldehyde decreased and benzoic acid increased. After 12 h of irradiation, toluene conversion reached 80%, with benzoic acid emerging as the predominant product (Fig. 4(c)). Even further oxidation of benzaldehyde happened under continuous irradiation, no CO_2 was detected as mineralized products. No significant decline in catalytic performance in five cycles (Fig. 4(d)), as well as no changes in crystal structure, morphology, element proportion and surface composition before and after recycling test underscored excellent stability of BOB/BMO-3 composite (Figs. S6–S8 and Table S1 in the ESM). The water promoted phenomenon was also found when the amount of toluene was varied (Fig. S9 in the ESM). Moreover, benzaldehyde production rate gradually increased with the amount of toluene increasing and BOB/BMO-3 exhibited superior photocatalytic oxidation performance in a mixed solvent of acetic acid and water, surpassing most of the reported photocatalysts (Table S2 in the ESM).

3.4 Photocatalytic mechanism analysis

To explore the reasons why water acts as a promoter, we compared the effects of water as an additive on the photocatalytic performance in different solvents. As depicted in Fig. 5(a), when water is added to the commonly involved solution for toluene selective oxidation system, there is a significant increase in photocatalytic activity only when acetic acid is used as solvent, whereas in other solvents it demonstrated a suppressive effect. When using trifluorotoluene and ethyl acetate as solvents, the limited solubility of water in these solvents hinders full contact between catalyst and toluene, leading to a decrease in catalytic activity. However, in acetonitrile, the introduction of water does not enhance photocatalytic activity either. Furthermore, adding a small amount of inorganic acid (0.2 mL of 0.1 M H_2SO_4, HCl, and HBr aqueous solution) to acetonitrile can significantly enhance the conversion of toluene. However, aqueous solutions of the corresponding inorganic salts (0.2 mL of 0.1 M Na_2SO_4, NaCl, and NaBr aqueous solution) have an inhibitory effect, which underscores the crucial role of an acidic environment in facilitating the conversion of toluene (Fig. S10 in the ESM). Considering the addition of water produces an acidic reaction environment which is favorable for H_2O_2 generation [19], we quantified H_2O_2 during photocatalytic process across various solvents. As depicted in Fig. 5(b), the introduction of water into an acetic acid medium substantially boosted the generation of H_2O_2. In contrast, the formation of H_2O_2 was negligible in a solvent mixture

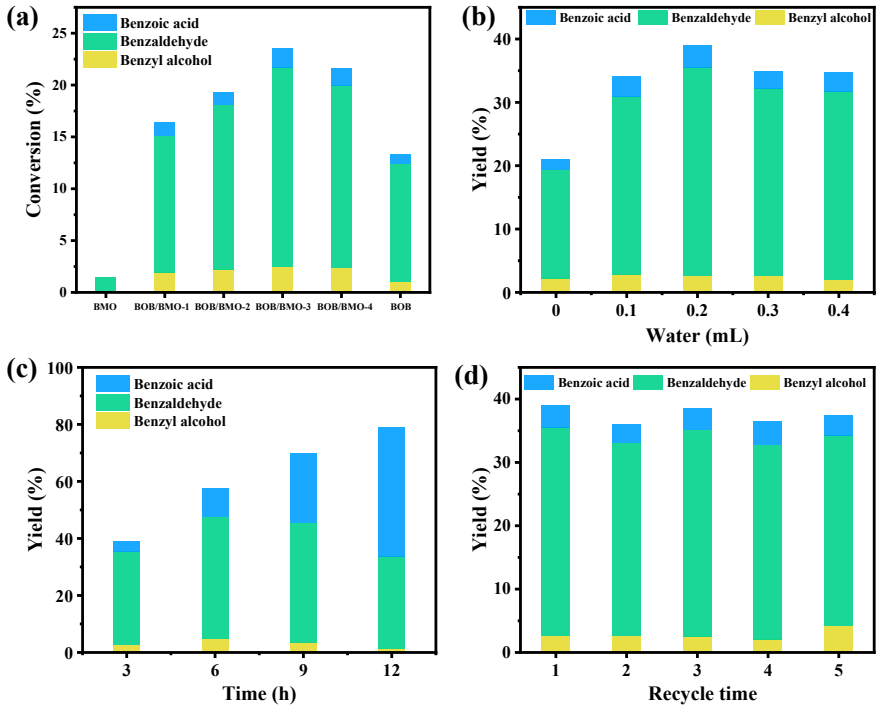

Figure 4 (a) Photocatalytic performance for toluene oxidation over prepared catalysts. Reaction conditions: 10 mg of photocatalyst, 50 μL of toluene, 2 mL of acetic acid, 1 atm O_2, $\lambda > 400$ nm, 3 h. (b) Effect of water content in acetic acid solvent on catalytic performance. (c) Time-dependent photocatalytic performance and (d) recycle property of BOB/BMO-3.

of acetonitrile and water. Additionally, a modest amount of H_2O_2 was observed in pure acetic acid solvent. These phenomena can likely be ascribed to the catalytic role of water generated during toluene oxidation process which enhanced H_2O_2 production.

ESR was used to identify ROS at different conditions (the ratio of solvent to water was 10:1, consistent with the photocatalytic reaction conditions) so as to understand the boosting of photocatalytic activity in the presence of H_2O as an additive in acetic acid solvent. When pristine acetic acid was used as solvent, $\cdot O_2^-$ as primary ROS was detected and its peak intensity increased by prolonging irradiation time (Fig. 5(c)). While in the acetic acid-water mixed solvent the predominant ROS was ·OH (Fig. 5(d)), which possesses higher oxidative ability compared to $\cdot O_2^-$, and it can directly activate the C(sp^3)–H bonds of toluene [5]. However, in acetonitrile-H_2O solution, $\cdot O_2^-$ and ·OH coexist, with $\cdot O_2^-$ being the dominant ROS species (Fig. 5(e)). Furthermore, the intensity of ·OH peak in acetic acid-water mixed solution is much higher than that in aqueous, indicating both acetic acid and H_2O played indispensable in promoting ·OH generation (Fig. 5(f)). It is deduced that the addition of water facilitates ionization of acetic acid, generating protons and creating an acidic environment and thus promotes the generation of ·OH. Based on the above results, we infer that when water is added to acetic acid, O_2 is reduced to H_2O_2 through a two-electron reduction process in the presence of H^+. Then H_2O_2 decompose to form ·OH, completing the transformation of $\cdot O_2^-$ to ·OH.

The impact of adding different radical trapping agents on reaction performance was shown in Fig. S11 in the ESM. Ammonium oxalate (AO), potassium persulfate ($K_2S_2O_8$), butylated hydroxytoluene (BHT), benzoquinone (BQ), and mannitol served as scavengers to quench h^+, e^-, carbon-centered radical, $\cdot O_2^-$, and ·OH, respectively. After the addition of AO, toluene still exhibited a conversion of 16.1%. It meant that holes are not the only active species responsible for the activation of C(sp^3)–H. H_2O_2 was detected in the catalytic process and its generation was not influenced by addition of AO (Fig. S12 in the ESM). The decomposition of H_2O_2 yields ·OH, which can activate the C(sp^3)–H bond of toluene, allowing toluene to maintain a certain conversion rate even when the holes were quenched. The reaction was suppressed to some extent when electron, $\cdot O_2^-$, or ·OH was quenched, suggesting they participate in this reaction. Upon quenching benzyl radical using BHT, the conversion rate of toluene exhibited a sharp decrease, underscoring the pivotal role of benzyl radical as an intermediate species, in agreement with our previous results [46–48]. Under N_2 or in dark conditions, toluene is essentially not converted, indicating that both O_2 and light irradiation are indispensable.

DFT was further used to compare the roles of $\cdot O_2^-$ and ·OH in the oxidation of toluene. When ·OH acts as ROS, due to their strong oxidizing nature, they can spontaneously activate toluene to benzyl radicals, with a ΔG of −0.06 eV. (Fig. 6(a)). Subsequently, the benzyls radical reacts with ·OH to form benzyl alcohol (ΔG = −2.42 eV), which then undergoes dehydrogenation to yield $C_6H_5CH_2O\cdot$ (ΔG = −0.25 eV). This intermediate subsequently reacts with ·OH to form $C_6H_5CH_2OOH$ (ΔG = −0.08 eV), and $C_6H_5CH_2OOH$ undergoes dehydration to produce benzaldehyde (ΔG = −2.40 eV). However, when the ROS is $\cdot O_2^-$, the activation of the C(sp^3)–H bonds in toluene by the photogenerated holes is more challenging and requires overcoming a larger reaction energy barrier (ΔG = 1.71 eV) (Fig. 6(b)). The benzyl radical combines with $\cdot O_2^-$ to form $*C_6H_5CH_2OO^-$, and $*C_6H_5CH_2OO^-$ spontaneously undergoes hydrogenation and dehydration to yield benzaldehyde. The overall ΔG for the entire reaction is −5.09 eV, which is lower than that when ·OH is the ROS at −5.25 eV. From the discussion above, it can be inferred that ·OH can significantly facilitate the C(sp^3)–H bonds cleavage of toluene to produce benzyl radicals, which can

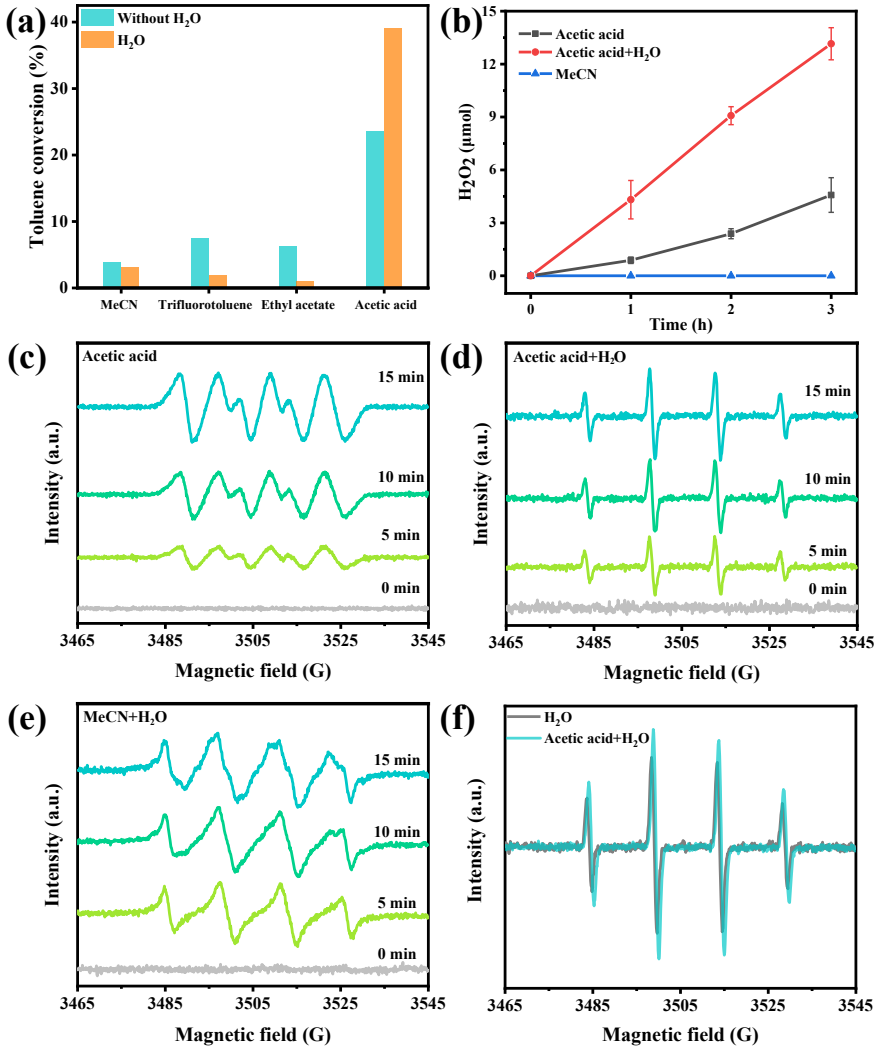

Figure 5 (a) Effect of solvent on photocatalytic performance of BOB/BMO-3. Reaction conditions: 10 mg of photocatalyst, 50 μL of toluene, 2 mL of solvent (0.2 mL of H_2O), 1 atm O_2, λ > 400 nm, 3 h. (b) Photocatalytic H_2O_2 production during the photocatalytic oxidation of toluene in different solvents. *In situ* EPR detection of BOB/BMO-3 in (c) acetic acid (d) acetic acid-water, and (e) acetonitrile-water. (f) *In situ* EPR detection of ·OH in pure water and acetic acid-water.

then undergo subsequent reactions to yield benzaldehyde. This result is consistent with the experimental findings and explains the reason for the enhanced oxidation performance of toluene when water is added to acetic acid.

Furthermore, *in situ* DRIFTS was provided to further reveal dynamic evolution of toluene on the surface of photocatalysts (Fig. 7(a)). The bands located at 3086, 3063 and 3029 cm^{-1} correspond to the C–H bond stretching vibration of the aromatic ring, while the band at 1604 and 1456 cm^{-1} belonged to the stretching vibration of C=C in aromatic rings [49, 50]. Meanwhile, the stretching vibration peaks of C(sp^3)–H (2933, 2869, 1456 and 1378 cm^{-1}) were observed, indicating the adsorption of toluene on the catalyst surface [51]. New bands at 1735 and 1704 cm^{-1} assignable to the C=O of benzaldehyde, gradually emerge under light irradiation and increase in intensity as the irradiation time was prolonged, providing evidence for the photocatalytic generation of benzaldehyde [52–54]. DRIFTS spectra of benzyl alcohol and benzaldehyde on the surface of BOB/BMO-3 were shown in Fig. S13 in the ESM. Within the wavenumber range of 1100–1250 cm^{-1}, the bands for benzaldehyde and benzyl alcohol on the catalyst surface are found to be in close proximity. Based on the findings reported in the literature, we attribute the bands observed at 1208 and 1177 cm^{-1} to the stretching vibrations of aromatic ring and side chain C–C stretching [55, 56]. Additionally, the bands at 1080 and 1029 cm^{-1} were attributed to the stretching vibrations of the C–O bond in benzyl alcohol, with their intensities increasing as the illumination time prolongs, which confirms the formation of benzyl alcohol during the reaction process [57, 58]. Based on all results above, we have proposed a mechanism for C(sp^3)–H activation and toluene transformation (Fig. 7(b)). On one hand, photogenerated holes activate toluene into benzyl radicals. On the other hand, in the presence of H_2O additive, an acidic chemical environment is established, which facilitates the generation of ·OH via a multi-electron reduction process (O_2 → $\cdot O_2^-$ → H_2O_2 → ·OH). Then ·OH dissociated C(sp^3)–H bonds of toluene directly into benzyl radicals. These benzyl radicals then engage in subsequent reactions with different ROS ($\cdot O_2^-$, ·OH, or O_2) to produce the desired products.

To demonstrate universality of this reaction system, photocatalytic performance of toluene derivatives with or without water was investigated (Table 1). Apparently, in the presence of water, conversion of all substrates is higher than that in the absence of water. At the same time, selectivity for the produced aldehydes

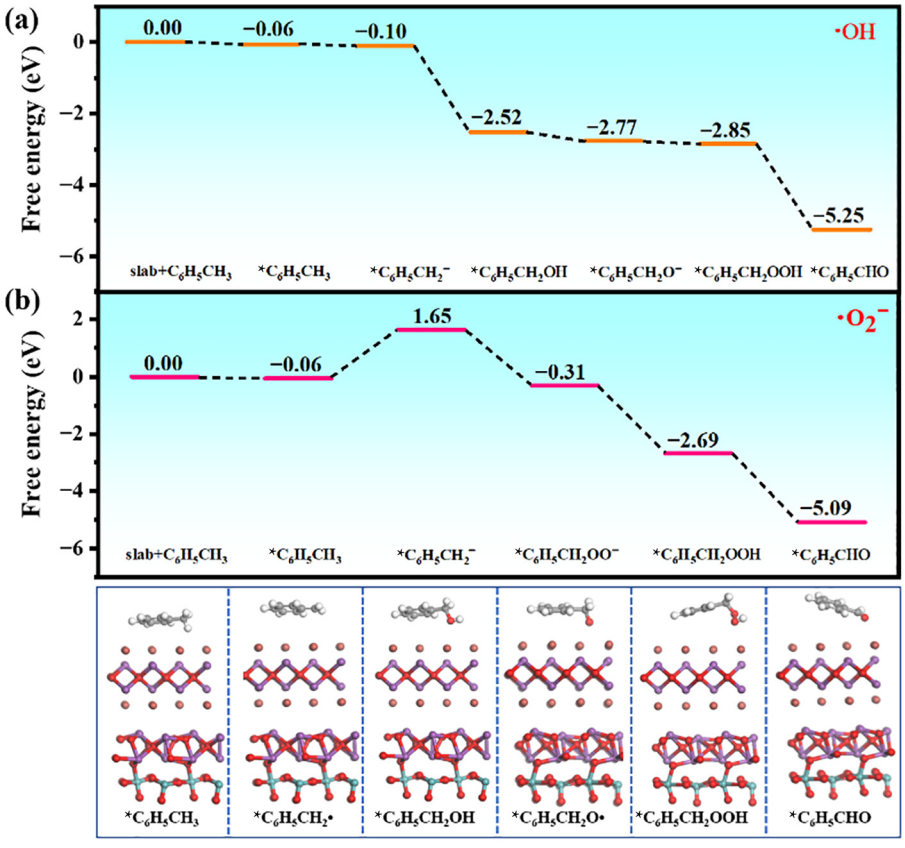

Figure 6 The pathways of toluene oxidation with different radicals (a) ·OH and (b) $\cdot O_2^-$.

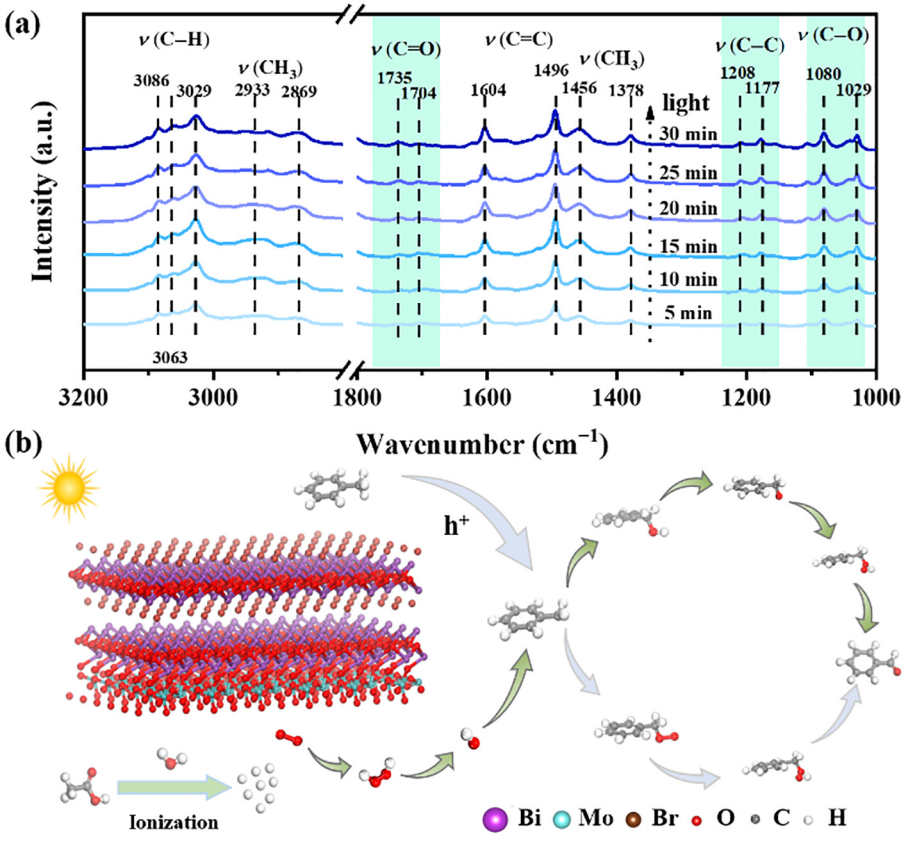

Figure 7 (a) *In situ* DRIFTS spectra of BOB/BMO-3 during the photocatalytic toluene oxidation process under visible light irradiation. (b) Schematic photocatalytic mechanism of toluene oxidation over the BOB/BMO-3 composite.

slightly increased, confirming addition of water enhances the photocatalytic performances of BOB/BMO-3 when acetic acid is used as solvent. The reactivity of p-substituted compounds was significantly enhanced relative to o- and m-substituted compounds due to the steric hindrance effect (entries 2–4). Compared to toluene derivatives with electron-withdrawing group at para-position, the ones with electron-donating group showed higher conversion (entries 4–10) due to electron-donating group facilitating the formation of carbon center radicals [8]. It is observed that there is certain linearity between the $\lg(k_X/k_H)$ values and the Brown–Okamoto constant (r+) from the Hammett plot of the oxidation of p-substituted toluene ($-CH_3$, $-C(CH_3)_3$, –H, –Cl, and $-CF_3$) (Fig. S14 in the ESM). The Hammett ρ value is estimated to be –0.83, which means toluene with electron-donating substituents will be more conducive to the advancement of the reaction [4, 5].

4 Conclusions

In summary, $BiOBr/Bi_2MoO_6$ Z-scheme heterostructure photocatalysts were synthesized through a one-step hydrothermal method. Good photocatalytic activity towards toluene oxidation into benzaldehyde was achieved in acetic acid solvent due to efficient separation of photogenerated charge carriers. When a proper amount of water as an additive was present, photocatalytic activity was doubled and selectivity for benzaldehyde also slightly improved. It was found water enhanced ionization of acetic acid, establishing an acidic chemical environment that benefited from the generation of reactive ·OH via the multi-electron reduction process ($O_2 \rightarrow \cdot O_2^- \rightarrow H_2O_2 \rightarrow \cdot OH$). Except for photogenerated holes, ·OH demonstrate a greater propensity for $C(sp^3)$–H bonds of toluene activation, which is the rate-determining step of this reaction, thereby contributed to a marked boosting in activity. This study provided a strategy to enhance photocatalytic activity by altering solvent to regulate ROS, which presents an encouraging avenue for improving efficiency of toluene oxidation reactions.

Electronic Supplementary Material: Supplementary material (SEM, XPS, Tauc plots, Mott–Schottky plots, catalyst structure model, used catalyst characterization, and controlled experiment) is available in the online version of this article at https://doi.org/10.26599/NR.2025.94907206.

Data availability

All data needed to support the conclusions in the paper are presented in the manuscript and the Electronic Supplementary Material. Additional data related to this paper may be requested from the corresponding author upon request.

Acknowledgements

This project was financially supported by the National Natural

Table 1 Photocatalytic performance of BOB/BMO-3 for selective oxidation of toluene derivatives[a]

Entry	Substrate	Without H_2O		With H_2O	
		Conversion (%)	Aldehyde selectivity (%)	Conversion (%)	Aldehyde selectivity (%)
1	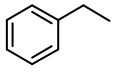	33.7	Acetophenone 96.5	54.0	Acetophenone 97.2
2		22.6	81.6	28.1	85.4
3	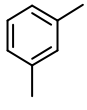	27.3	88.2	36.4	92.6
4	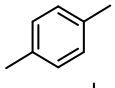	29.0	93.6	49.4	95.4
5	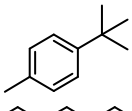	38.4	86.6	62.2	87.9
6	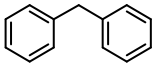	27.0	88.9	35.5	89.2
7	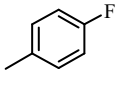	19.4	85.1	34.2	87.2
8	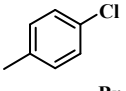	26.9	92.2	32.9	95.6
9	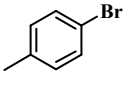	24.8	81.8	47.8	84.4
10	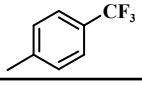	4.0	100	9.2	100

[a]Reaction conditions: 10 mg of photocatalyst, 0.5 mmol of substrate, 2 mL of acetic acid (0.2 mL of H_2O), 1 atm O_2 under visible light ($\lambda > 400$ nm) for 3 h.

Science Foundation of China (Nos. 22322804, 21938002, and 22278119).

Declaration of competing interest

All the contributing authors report no conflict of interests in this work.

Author contribution statement

S. T.: Experimental conducting, writing draft, theoretical calculation. J. X. L.: Experimental conducting, formal analysis, data curation. B. H. W.: Formal analysis, data curation. X. W.: Formal analysis, data curation. X. S. H.: Formal analysis, data curation. H. J. W.: Discussion, revision. L. C.: Funding acquisition, supervision, writing-guidance. S.-F. Y.: Funding acquisition, supervision, revision.

Use of AI statement

None.

References

[1] Labinger, J. A.; Bercaw, J. E. Understanding and exploiting C–H bond activation. *Nature* **2002**, *417*, 507–514.

[2] Kesavan, L.; Tiruvalam, R.; Ab Rahim, M. H.; Bin Saiman, M. I.; Enache, D. I.; Jenkins, R. L.; Dimitratos, N.; Lopez-Sanchez, J. A.; Taylor, S. H.; Knight, D. W. et al. Solvent-free oxidation of primary carbon-hydrogen bonds in toluene using Au-Pd alloy nanoparticles. *Science* **2011**, *331*, 195–199.

[3] Rogge, T.; Kaplaneris, N.; Chatani, N.; Kim, J.; Chang, S.; Punji, B.; Schafer, L. L.; Musaev, D. G.; Wencel-Delord, J.; Roberts, C. A. et al. C–H activation. *Nat. Rev. Methods Primers* **2021**, *1*, 43.

[4] Yang, Y. L.; Chen, Z. Y.; Huang, H. L.; Liu, Y. X.; Zou, J. H.; Shen, S. Q.; Yan, J. W.; Zhang, J. S.; Zhuang, Z. Y.; Luo, Z. Z. et al. Synergistic surface activation during photocatalysis on perovskite derivative sites in heterojunction. *Appl. Catal. B: Environ.* **2023**, *323*, 122146.

[5] Zhou, B.; Fan, K. Z.; Chong, Y. A.; Xu, S.; Wei, J. W.; Wei, J. K.; Sergeev, A. A.; Wong, K. S.; Li, T.; Chen, G. X. et al. Modulating adsorption-redox sites and charge separation of $Cs_3Bi_2Br_{9-x}$@AgBr core–shell heterostructure for selective toluene photooxidation. *ACS Energy Lett.* **2024**, *9*, 1743–1752.

[6] Xiong, L. Q.; Tang, J. W. Strategies and challenges on selectivity of photocatalytic oxidation of organic substances. *Adv. Energy Mater.* **2021**, *11*, 2003216.

[7] Xu, X.; Wang, J.; Chen, T.; Yang, N.; Wang, S. Y.; Ding, X.; Chen, H. Deep insight into ROS mediated direct and hydroxylated dichlorination process for efficient photocatalytic sodium pentachlorophenate mineralization. *Appl. Catal. B: Environ.* **2021**, *296*, 120352.

[8] Bai, Z. J.; Tan, X. P.; Chen, L.; Hu, B.; Tan, Y. X.; Mao, Y.; Shen, S.; Guo, J. K.; Au, C. T.; Liang, Z. W. et al. Efficient photocatalytic toluene selective oxidation over $Cs_3Bi_{1.8}Sb_{0.2}Br_9$ nanosheets: Enhanced charge carriers generation and C–H bond dissociation. *Chem. Eng. Sci.* **2022**, *247*, 116983.

[9] Tan, Y. X.; Chai, Z. M.; Wang, B. H.; Tian, S.; Deng, X. X.; Bai, Z. J.; Chen, L.; Shen, S.; Guo, J. K.; Cai, M. Q. et al. Boosted photocatalytic oxidation of toluene into benzaldehyde on $CdIn_2S_4$-CdS: Synergetic effect of compact heterojunction and S-vacancy. *ACS Catal.* **2021**, *11*, 2492–2503.

[10] Li, Z. Z.; Meng, X. C. New insight into reactive oxidation species (ROS) for bismuth-based photocatalysis in phenol removal. *J. Hazard. Mater.* **2020**, *399*, 122939.

[11] Ma, H. Y.; Zhao, L. X.; Guo, L. H.; Zhang, H.; Chen, F. J.; Yu, W. C. Roles of reactive oxygen species (ROS) in the photocatalytic degradation of pentachlorophenol and its main toxic intermediates by TiO_2/UV. *J. Hazard. Mater.* **2019**, *369*, 719–726.

[12] Nosaka, Y.; Nosaka, A. Y. Generation and detection of reactive oxygen species in photocatalysis. *Chem. Rev.* **2017**, *117*, 11302–11336.

[13] Xu, C. Y.; Pan, Y. T.; Wan, G.; Liu, H.; Wang, L.; Zhou, H.; Yu, S. H.; Jiang, H. L. Turning on visible-light photocatalytic C–H oxidation over metal-organic frameworks by introducing metal-to-cluster charge transfer. *J. Am. Chem. Soc.* **2019**, *141*, 19110–19117.

[14] Cao, X.; Huang, A. J.; Liang, C.; Chen, H. C.; Han, T.; Lin, R.; Peng, Q.; Zhuang, Z. W.; Shen, R. A.; Chen, H. M. et al. Engineering lattice disorder on a photocatalyst: Photochromic BiOBr nanosheets enhance activation of aromatic C–H Bonds via water oxidation. *J. Am. Chem. Soc.* **2022**, *144*, 3386–3397.

[15] Wang, C. Y.; Zhang, X.; Zhang, Y. J.; Chen, J. J.; Huang, G. X.; Jiang, J.; Wang, W. K.; Yu, H. Q. Direct generation of hydroxyl radicals over bismuth oxybromide nanobelts with tuned band structure for photocatalytic pollutant degradation under visible light irradiation. *Appl. Catal. B: Environ.* **2018**, *237*, 464–472.

[16] Wang, Y. X.; Li, X.; Liu, S. N.; Liu, Y.; Kong, T.; Zhang, H. Y.; Duan, X. G.; Chen, C. M.; Wang, S. B. Roles of catalyst structure and gas surface reaction in the generation of hydroxyl radicals for photocatalytic oxidation. *ACS Catal.* **2022**, *12*, 2770–2780.

[17] Devi, M.; Chakraborty, D.; Barbhuiya, M. H.; Das, B.; Nath, S.; Dhar, S. S. Phase engineering in graphitic carbon nitride with imidazolium sulfonic acid chloride ionic liquid functionalization for photocatalytic side-chain oxidation of toluene. *Appl. Catal. A: Gen.* **2022**, *633*, 118515.

[18] Lu, B.; Cai, N.; Sun, J.; Wang, X.; Li, X.; Zhao, J. X.; Cai, Q. H. Solvent-free oxidation of toluene in an ionic liquid with H_2O_2 as oxidant. *Chem. Eng. J.* **2013**, *225*, 266–270.

[19] Zhang, Q. H.; An, B.; Lei, Y.; Gao, Z. X.; Zhang, H. N.; Xue, S.; Jin, X.; Xu, W. G.; Wu, Z. H.; Wu, M. B. et al. $Cl_2^{\cdot-}$ mediates direct and selective conversion of inert C(sp^3)–H bonds into aldehydes/ketones. *Angew. Chem., Int. Ed.* **2023**, *62*, e202304699.

[20] Chen, X.; Sheng, X.; Zhou, H.; Liu, Z. P.; Xu, M. M.; Feng, X. J. Hydrophobicity promoted efficient hydroxyl radical generation in visible-light-driven photocatalytic oxidation. *Small* **2024**, *20*, e2310128.

[21] Kondo, Y.; Honda, K.; Kuwahara, Y.; Mori, K.; Kobayashi, H.; Yamashita, H. Boosting photocatalytic hydrogen peroxide production from oxygen and water using a hafnium-based metal-organic framework with missing-linker defects and nickel single atoms. *ACS Catal.* **2022**, *12*, 14825–14835.

[22] Xia, H.; Liu, Z. L.; Xu, Y. Y.; Zuo, J. L.; Qin, Z. Z. Highly efficient V–Mo–Fe–O catalysts for selective oxidation of toluene to benzaldehyde. *Catal. Commun.* **2016**, *86*, 72–76.

[23] Wu, X. L.; Tan, H. L.; Zhang, C. H.; Teng, Z. Y.; Liu, Z. L.; Hau Ng, Y.; Zhang, Q. T.; Su, C. L. Recent advances in two-dimensional ultrathin Bi-based photocatalysts. *Prog. Mater. Sci.* **2023**, *133*, 101047.

[24] Ma, H.; He, Y.; Chen, P.; Wang, H.; Sun, Y. J.; Li, J. Y.; Dong, F.; Xie, G. X.; Sheng, J. P. Ultrathin two-dimensional Bi-based photocatalysts: Synthetic strategies, surface defects, and reaction mechanisms. *Chem. Eng. J.* **2021**, *417*, 129305.

[25] Sun, Y.; Ahmadi, Y.; Kim, K. H.; Lee, J. The use of bismuth-based photocatalysts for the production of ammonia through photocatalytic nitrogen fixation. *Renew. Sustain. Energy Rev.* **2022**, *170*, 112967.

[26] Yu, H. B.; Jiang, L. B.; Wang, H.; Huang, B. B.; Yuan, X. Z.; Huang, J. H.; Zhang, J.; Zeng, G. M. Modulation of Bi_2MoO_6-based materials for photocatalytic water splitting and environmental application: A critical review. *Small* **2019**, *15*, 1901008.

[27] Zhao, Q. Y.; Hou, X. L.; Liu, X. L.; Chong, M. B.; Cheng, D. G.; Chen, F. Q.; Zhan, X. L. Facet-dependent oxygen mobility and reaction pathways for oxidative dehydrogenation of 1-butene over Bi_2MoO_6. *ACS Catal.* **2024**, *14*, 3543–3555.

[28] Chen, H. J.; Xu, R. H.; Chen, D.; Lu, T. L.; Li, H. J.; Wang, M.

Subsurface Mo vacancy in bismuth molybdate promotes photocatalytic oxidation of lactate to pyruvate. *ACS Catal.* **2024**, *14*, 1977–1986.
[29] Ding, F.; Chen, P.; Liu, F.; Chen, L.; Guo, J. K.; Shen, S.; Zhang, Q.; Meng, L. H.; Au, C. T.; Yin, S. F. Bi_2MoO_6/g-C_3N_4 of 0D/2D heterostructure as efficient photocatalyst for selective oxidation of aromatic alkanes. *Appl. Surf. Sci.* **2019**, *490*, 102–108.
[30] Cai, K.; Lv, S. Y.; Song, L. N.; Chen, L.; He, J.; Chen, P.; Au, C. T.; Yin, S. F. Facile preparation of ultrathin Bi_2MoO_6 nanosheets for photocatalytic oxidation of toluene to benzaldehyde under visible light irradiation. *J. Solid State Chem.* **2019**, *269*, 145–150.
[31] Zhang, K. F.; Chen, H. X.; Liu, Y. X.; Deng, J. G.; Jing, L.; Rastegarpanah, A.; Pei, W. B.; Han, Z.; Dai, H. X. Two-dimensional $Bi_2W_xMo_{1-x}O_6$ solid solution nanosheets for enhanced photocatalytic toluene oxidation to benzaldehyde. *Appl. Catal. B: Environ.* **2022**, *315*, 121545.
[32] Hao, Y. C.; Dong, X. L.; Wang, X. Y.; Zhai, S. R.; Ma, H. C.; Zhang, X. F. Controllable electrostatic self-assembly of sub-3 nm graphene quantum dots incorporated into mesoporous Bi_2MoO_6 frameworks: Efficient physical and chemical simultaneous co-catalysis for photocatalytic oxidation. *J. Mater. Chem. A.* **2016**, *4*, 8298–8307.
[33] Chen, C.; Qiu, G. H.; Wang, T.; Zheng, Z. Q.; Huang, M. T.; Li, B. X. Modulating oxygen vacancies on bismuth-molybdate hierarchical hollow microspheres for photocatalytic selective alcohol oxidation with hydrogen peroxide production. *J. Colloid Interface Sci.* **2021**, *592*, 1–12.
[34] Kresse, G.; Furthmüller, J. Efficiency of *ab-initio* total energy calculations for metals and semiconductors using a plane-wave basis set. *Comput. Mater. Sci.* **1996**, *6*, 15–50.
[35] Kresse, G.; Joubert, D. From ultrasoft pseudopotentials to the projector augmented-wave method. *Phys. Rev. B* **1999**, *59*, 1758–1775.
[36] Perdew, J. P.; Burke, K.; Ernzerhof, M. Generalized gradient approximation made simple. *Phys. Rev. Lett.* **1996**, *77*, 3865–3868.
[37] Ma, T. X.; Yang, C. M.; Guo, L.; Soomro, R. A.; Wang, D. J.; Xu, B.; Fu, F. Refining electronic properties of Bi_2MoO_6 by In-doping for boosting overall nitrogen fixation via relay catalysis. *Appl. Catal. B: Environ.* **2023**, *330*, 122643.
[38] Liu, Z.; Tian, J.; Yu, C. L.; Fan, Q. Z.; Liu, X. Q. Solvothermal fabrication of Bi_2MoO_6 nanocrystals with tunable oxygen vacancies and excellent photocatalytic oxidation performance in quinoline production and antibiotics degradation. *Chin. J. Catal.* **2022**, *43*, 472–484.
[39] Jing, K. Q.; Xiong, J. H.; Qin, N.; Song, Y. J.; Li, L. Y.; Yu, Y.; Liang, S. J.; Wu, L. Development and photocatalytic mechanism of monolayer Bi_2MoO_6 nanosheets for the selective oxidation of benzylic alcohols. *Chem. Commun.* **2017**, *53*, 8604–8607.
[40] Zheng, Y.; Zhou, T. F.; Zhao, X. D.; Pang, W. K.; Gao, H.; Li, S. A.; Zhou, Z.; Liu, H. K.; Guo, Z. P. Atomic interface engineering and electric-field effect in ultrathin Bi_2MoO_6 nanosheets for superior lithium ion storage. *Adv. Mater.* **2017**, *29*, 1700396.
[41] Feng, R. Z.; Guo, M. N.; Yang, Z. Q.; Qiu, J. Q.; Wang, Z. Q.; Zhao, Y. L. 0D/2D Bi_2MoO_6 quantum dots/rGO heterojunction boosting full solar spectrum-driven photothermal catalytic CO_2 reduction to solar fuels. *Carbon* **2024**, *224*, 119079.
[42] Tian, S.; Ding, Y. F.; Cai, M. Q.; Chen, L.; Au, C. T.; Yin, S. F. Enhanced photocatalytic activity of the direct Z-scheme black phosphorus/BiOX (X = Cl, Br, I) heterostructures. *Phys. Chem. Chem. Phys.* **2021**, *23*, 17894–17903.
[43] Zhang, J. R.; Deng, X. Z.; Gao, B.; Chen, L.; Au, C. T.; Li, K. L.; Yin, S. F.; Cai, M. Q. Theoretical study on the intrinsic properties of In_2Se_3/MoS_2 as a photocatalyst driven by near-infrared, visible and ultraviolet light. *Catal. Sci. Technol.* **2019**, *9*, 4659–4667.
[44] Yang, X. M.; Wang, X. N.; Liang, C. H.; Su, W. G.; Wang, C.; Feng, Z. C.; Li, C.; Qiu, J. S. Aerobic oxidation of alcohols over Au/TiO_2: An insight on the promotion effect of water on the catalytic activity of Au/TiO_2. *Catal. Commun.* **2008**, *9*, 2278–2281.
[45] Wei, Q. B.; Yu, C.; Song, X. D.; Zhong, Y. P.; Ni, L.; Ren, Y. W.; Guo, W.; Yu, J. H.; Qiu, J. S. Recognition of water-induced effects toward enhanced interaction between catalyst and reactant in alcohol oxidation. *J. Am. Chem. Soc.* **2021**, *143*, 6071–6078.
[46] Bai, Z. J.; Mao, Y.; Wang, B. H.; Chen, L.; Tian, S.; Hu, B.; Li, Y. J.; Au, C. T.; Yin, S. F. Tuning photocatalytic performance of $Cs_3Bi_2Br_9$ perovskite by g-C_3N_4 for C(sp^3)–H bond activation. *Nano Res.* **2023**, *16*, 6104–6112.
[47] Chai, Z. M.; Wang, B. H.; Tan, Y. X.; Bai, Z. J.; Pan, J. B.; Chen, L.; Shen, S.; Guo, J. K.; Xie, T. L.; Au, C. T. et al. Enhanced photocatalytic activity for selective oxidation of toluene over cubic-hexagonal CdS phase junctions. *Ind. Eng. Chem. Res.* **2021**, *60*, 11106–11116.
[48] Deng, X. X.; Tian, S.; Chai, Z. M.; Bai, Z. J.; Tan, Y. X.; Chen, L.; Guo, J. K.; Shen, S.; Cai, M. Q.; Au, C. T. et al. Boosted activity for toluene selective photooxidation over Fe-doped Bi_2WO_6. *Ind. Eng. Chem. Res.* **2020**, *59*, 13528–13538.
[49] Jiang, Y.; Jiang, Y. S.; Cheng, S. Y.; Xi, Y. Y.; Sun, X.; Xu, Y. C.; Yang, Z. D. Modulate synthesis of CeMn solid solution using various alcohols for toluene catalytic oxidation: Synergistic effect of Ce–Mn and reaction mechanism. *J. Hazard. Mater.* **2024**, *476*, 135051.
[50] Mi, R. L.; Li, D.; Hu, Z.; Yang, R. T. Morphology effects of CeO_2 nanomaterials on the catalytic combustion of toluene: A combined kinetics and diffuse reflectance infrared fourier transform spectroscopy study. *ACS Catal.* **2021**, *11*, 7876–7889.
[51] Xue, Z.; Yang, J. R.; Ma, L. N.; Li, H. C.; Luo, L.; Ji, K. Y.; Li, Z. H.; Kong, X. G.; Shao, M. F.; Zheng, L. R. et al. Efficient benzylic C–H bond activation over single-atom yttrium supported on TiO_2 via facilitated molecular oxygen and surface lattice oxygen activation. *ACS Catal.* **2024**, *14*, 249–261.
[52] Shi, Y. Z.; Li, P.; Chen, H. L.; Wang, Z. W.; Song, Y. J.; Tang, Y.; Lin, S.; Yu, Z. Y.; Wu, L.; Yu, J. C. et al. Photocatalytic toluene oxidation with nickel-mediated cascaded active units over Ni/Bi_2WO_6 monolayers. *Nat. Commun.* **2024**, *15*, 4641.
[53] Li, S. Z.; Huber, N.; Huang, W.; Wei, W. X.; Landfester, K.; Ferguson, C. T. J.; Zhao, Y.; Zhang, K. A. I. Triazine frameworks for the photocatalytic selective oxidation of toluene. *Angew. Chem., Int. Ed.* **2024**, *63*, e202400101.
[54] Zhang, Q. L.; Yang, S. Y.; Zhang, H. X.; He, T. Y.; Liu, W. M.; Sun, X. M.; Li, G. B.; Yu, Y. B.; Peng, H. G. Unveiling the confinement and interface effect on low temperature degradation of toluene over mesoporous zeolite encapsulated Pt-CeO_2 catalyst. *Chem. Eng. J.* **2024**, *485*, 150004.
[55] Li, Y. F.; Chen, T. Y.; Zhao, S. Q.; Wu, P.; Chong, Y. N.; Li, A. Q.; Zhao, Y.; Chen, G. X.; Jin, X. J.; Qiu, Y. C. et al. Engineering cobalt oxide with coexisting cobalt defects and oxygen vacancies for enhanced catalytic oxidation of toluene. *ACS Catal.* **2022**, *12*, 4906–4917.
[56] Zhao, J. G.; Wang, P. F.; Wang, J.; Liu, C. L.; Wang, J. L.; Shi, L.; Xu, G. W.; Abudula, A.; Guan, G. Q. Biostarch-assisted synthesis of microscopic heterogeneous manganese-cobalt oxides for efficient catalytic combustion of toluene. *Chem. Eng. J.* **2023**, *464*, 142739.
[57] Li, B.; Xiong, H.; Dai, W. L.; Huang, Z. L.; Zhong, X. L.; Zhang, J.; Zhou, L.; Wu, K. S.; Zou, J. P.; Luo, X. B. Enabling the activation of lattice oxygen and high distribution of Co^{3+} on $LaCoO_3$ surface through fluorine incorporation to promote toluene combustion. *Appl. Catal. B: Environ. Energy.* **2024**, *347*, 123828.
[58] Chong, Y. N.; Chen, T. Y.; Li, Y. F.; Lin, J. J.; Huang, W. H.; Chen, C. L.; Jin, X. J.; Fu, M. L.; Zhao, Y.; Chen, G. X. et al. Quenching-induced defect-rich platinum/metal oxide catalysts promote catalytic oxidation. *Environ. Sci. Technol.* **2023**, *57*, 5831–5840.